

Accurate Relativistic Real-Time Time-Dependent Density Functional Theory for Valence and Core Attosecond Transient Absorption Spectroscopy

Torsha Moitra,[†] Lukas Konecny,^{†,‡} Marius Kadek,^{†,¶,§} Angel Rubio,^{‡,||,⊥} and
Michal Repisky^{*,†,#}

[†]*Hylleraas Centre for Quantum Molecular Sciences, Department of Chemistry, UiT The Arctic University of Norway, 9037 Tromsø, Norway*

[‡]*Max Planck Institute for the Structure and Dynamics of Matter, Center for Free Electron Laser Science, Luruper Chaussee 149, 22761 Hamburg, Germany*

[¶]*Department of Physics, Northeastern University, Boston, Massachusetts 02115, USA*

[§]*Algorithmiq Ltd., Kanavakatu 3C, FI-00160 Helsinki, Finland*

^{||}*Center for Computational Quantum Physics (CCQ), The Flatiron Institute, 162 Fifth Avenue, New York, New York 10010, USA*

[⊥]*Nano-Bio Spectroscopy Group, Departamento de Física de Materiales, Universidad del País Vasco, 20018 San Sebastian, Spain*

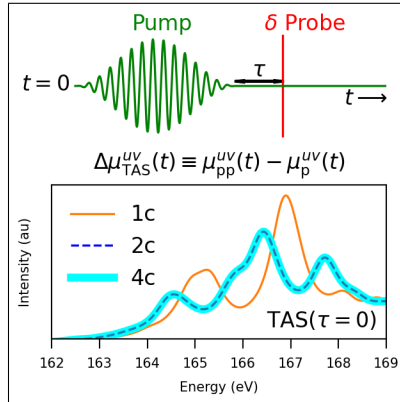
[#]*Department of Physical and Theoretical Chemistry, Faculty of Natural Sciences, Comenius University, 81499 Bratislava, Slovakia*

E-mail: michal.repisky@uit.no

Abstract

First principle theoretical modeling of out-of-equilibrium processes observed in attosecond pump-probe transient absorption spectroscopy (TAS) triggering pure electron dynamics remains a challenging task, specially for heavy elements and/or core excitations containing fingerprints of scalar and spin-orbit relativistic effects. To address this, we formulate a methodology for simulating TAS within the relativistic real-time time-dependent density functional theory (RT-TDDFT) framework, for both the valence and core energy regime. Especially for TAS, full four-component (4c) RT simulations are feasible but computationally demanding. Therefore, in addition to the 4c approach, we also introduce the atomic mean-field exact two-component (amfX2C) Hamiltonian accounting for one- and two-electron picture-change corrections within RT-TDDFT. amfX2C preserves the accuracy of the parent 4c method at a fraction of its computational cost. Finally, we apply the methodology to study valence and near L_{2,3}-edge TAS processes of experimentally relevant systems and provide additional physical insights using relativistic non-equilibrium response theory.

Graphical TOC Entry



Transient absorption spectroscopy (TAS) is a powerful non-linear technique for investigating ultrafast state-resolved processes and electronic superposition using two pulses, *viz* pump and time-delayed probe pulse.¹⁻³ TAS offers additional degrees of freedom, namely, pump field features like shape, amplitude, carrier frequency, direction, and pump-probe time delays, absent in conventional spectroscopy. Of which, the effect of time-delay between the pulses is most commonly followed experimentally.^{4,5} Since long, the emphasis has been on the femto- to pico-second timescales, which involved time-resolving processes initiated by nuclear motions.⁶⁻⁹ However, with the advent of atto-second pulses, there has been an ever increasing interest in studying sub-femtosecond timescale processes, focusing on the motion of electrons on their natural time-scale, with minimal influence of nuclear degrees of freedom.^{2,10-19} Simultaneously, generation of intense isolated soft X-ray free electron laser pulses with sub-femtosecond temporal widths has been achieved recently, promoting investigations of attosecond resolved spectroscopies involving core orbitals.^{20,21} Due to their characteristic element specificity and unprecedented temporal resolution, ultrafast X-ray spectroscopies are emerging as indispensable tools for biological and material sciences.^{22,23} Especially X-ray transient absorption spectroscopy (XTAS) which employs short X-ray probe pulses is now extensively being used to investigate electron dynamics of molecules and solid-state systems.^{7,22-27} This dictates the need to develop reliable theoretical tools to aid the interpretation and prediction of such phenomena.

With regards to simulating the response of the laser pulses relevant to pump-probe spectroscopies, real-time (RT) formalism offers a straightforward approach²⁸⁻⁴⁶ over response theory based methods as the former is applicable for a large range of field intensities, and resembles the experimental setup in a natural way. Addressing core level spectroscopies has added complexities, as it requires the inclusion of scalar (SC) and spin-orbit (SO) relativistic effects, which are most reliably described by multi-component relativistic quantum chemical methods. Here, the “gold standard” is the four-component (4c) methodology including both SC and SO effects variationally via the one-electron Dirac Hamiltonian in combination with

instantaneous Coulomb interactions among the particles. Since the 4c treatment can be time consuming, especially for RT simulations, researchers have focused on the development of approximate 2c Hamiltonians.⁴⁷ An approach that has gained wide popularity in recent years is the exact two-component (X2C) Hamiltonian as it reduces the original 4c problem by half, requiring only a few simple algebraic manipulations.^{48–53} There exist several variants of X2C Hamiltonian, ranging from a pure one-electron X2C (1eX2C) Hamiltonian where two-electron (2e) interactions are entirely omitted from the X2C decoupling transformation,^{47,54} to a molecular mean-field X2C (mmfX2C) Hamiltonian where the decoupling is performed *after* 4c molecular self-consistent field (SCF) calculations.⁵⁵ Inbetween there are several X2C Hamiltonian models that extend 1eX2C by including 2e interactions approximately via (i) element and angular-momentum specific screening factors in the evaluation of one-electron SO integrals;^{56,57} (ii) a mean-field SO approach⁵⁸ which has been the basis for the widely popular AMFI module;⁵⁹ and (iii) an approach that exploits atomic model densities obtained within the framework of Kohn–Sham DFT.^{60,61} The screening factors of type (i) are sometimes referred to as “Boettger factors” or as the (modified) screened–nuclear–spin–orbit approach ((m)SNSO).^{62,63} Recently, an atomic mean-field (amfX2C) as well as an extended atomic mean-field (eamfX2C) approach have been presented within the X2C framework,⁶⁴ extending some of earlier ideas of Liu and Cheng⁶⁵ by comprising the full 2e SO and SC corrections, regardless whether they arise from the Coulomb, Coulomb–Gaunt, or Coulomb–Breit Hamiltonian. Moreover, this ansatz takes into account the characteristics of the underlying correlation framework, *viz.*, wave-function theory or (KS-)DFT, which enables tailor-made exchange–correlation (xc) corrections to be introduced.⁶⁴ While all above mentioned relativistic methods lie within the static time-independent regime, extensions to the RT framework⁶⁶ were recently formulated both at 4c^{67–69} and 2c^{54,70,71} level.

In this letter, we present a novel theoretical methodology to address several fascinating characteristics associated with TAS and its simulation. First, to understand the physics governing TAS, we generalize the non-equilibrium response theory formalism to incorporate

complex orbitals necessary for relativistic theory. This facilitates us to interpret unique spectral observations inherent to TAS. Next, to provide first-principle computational approach for simulation of TAS across the entire Periodic Table and/or core atomic region(s), we implement a relativistic variant of RT time-dependent density functional theory (TDDFT) based on 4c Dirac–Coulomb Hamiltonian. This allows us to account for SC and SO relativistic effects variationally, thereby significantly broadening the applicability of the tool. Since the gold standard 4c method is still computationally demanding and popular one-electron 1eX2C is not sufficiently accurate in comparison to its 4c reference,⁷² finally we formulate and implement for the first time a simple yet numerically accurate amfX2C Hamiltonian in context of RT framework. It incorporates all spin-free and spin-dependent relativistic picture-change corrections originating from X2C transformation, giving remarkable agreement with reference 4c results. Consequently, we apply the amfX2C Hamiltonian to provide physical insights into TAS near valence and L_{2,3}-edge for experimentally relevant systems.

In order to lay the theoretical foundations for describing pump-probe spectroscopy, we consider in this work the non-overlapping regime, in which the probe field/pulse $\mathcal{F}(t)$ is applied at or after the end of the pump pulse $\mathcal{E}(t)$. The pump pulse takes the form

$$\mathcal{E}(t) = \mathbf{n}\mathcal{E}(t) = \mathbf{n}\mathcal{E}_0 \cos^2\left(\pi\frac{t-t_0}{T}\right) \sin(\omega_0 t + \phi), \quad (1)$$

and is characterized by the amplitude \mathcal{E}_0 , shape (\cos^2 -enveloped sin function), carrier frequency ω_0 , time duration T , carrier-envelope phase (CEP) ϕ , and polarization along the unit vector \mathbf{n} . The pump pulse is centered at t_0 , and is zero (inactive) outside of the window of size T , *i.e.* for $t < t_0 - \frac{T}{2}$ and $t > t_0 + \frac{T}{2}$. In practice, the duration of the pump is chosen to be an integer number of carrier periods and the time $t = 0$ corresponds to the onset of the pump, *i.e.* $t_0 = \frac{T}{2}$, and the CEP is set to 0. For the probe pulse, we use the analytical form of a delta field⁶⁷

$$\mathcal{F}(t) = \mathbf{m}\mathcal{F}(t) = \mathbf{m}\mathcal{F}_0\delta(t - (T + \tau)), \quad (2)$$

characterized by its amplitude \mathcal{F}_0 , polarization direction \mathbf{m} , and positioned at $T + \tau$, where τ is a time-delay between pump and probe pulse.

To get physical insight into pump–probe processes, it is instructive to examine them from the point of non-equilibrium response theory.⁷³ First, we derive the non-perturbative form of the response to the probe field applied to the non-stationary (out-of-equilibrium) state $|\Psi[\mathcal{E}]\rangle$ generated by the previous pump pulse lasting from time 0 to T . The time evolution of a system after the end of the pump is described by the Hamiltonian,

$$\hat{H}(t) = \hat{H}_0 - \sum_{u \in x,y,z} \mathcal{F}_u(t) \hat{P}_u; \quad \hat{P}_u = - \sum_{i=1}^N \hat{r}_{i,u}, \quad (3)$$

where \hat{H}_0 is the static Hamiltonian describing the N electron system itself, and $\sum_{u \in x,y,z} \mathcal{F}_u(t) \hat{P}_u$ denotes the coupling of the molecular system to the probe pulse via the electric dipole operator $\hat{\mathbf{P}}$. Note that we have assumed the dipole approximation and we work in the length gauge all over the paper. The wave function $|\Psi(t)\rangle$ for times $t > T + \tau$ can be expressed using unitary evolution operators⁷⁴ that propagate the state $|\Psi[\mathcal{E}]\rangle$ from the time $t = T$. To isolate the singularity caused by the δ -type probe pulse, we split the time propagation into three parts using a sequence of evolution operators. First, we propagate from the time $t = T$ to $t = T + \tau$. Here, the evolution operator has the simple form of $e^{-i\hat{H}_0\tau}$ (where T cancelled out), since both the pump and probe pulses are not active in this interval, and the time propagation is determined only by the static Hamiltonian \hat{H}_0 . Second, we handle the probe perturbation by propagating the wave function on the infinitesimal time interval from $t = T + \tau - \epsilon$ to $t = T + \tau + \epsilon$ as $\epsilon \rightarrow 0$. Such a “step” propagation can be expressed in the closed form⁶⁷ as $e^{-i\hat{Q}_v}$, where $\hat{Q}_v \equiv -\mathcal{F}_0 \hat{P}_v$. Third, the evolution from $t = T + \tau$ to an arbitrary t is, like in the first case, determined by the static Hamiltonian as $e^{-i\hat{H}_0(t-T-\tau)}$. Hence, the wave function is given by

$$|\Psi(t)\rangle = e^{-i\hat{H}_0(t-T-\tau)} e^{-i\hat{Q}_v} e^{-i\hat{H}_0\tau} |\Psi[\mathcal{E}]\rangle. \quad (4)$$

In the basis of stationary eigenstates $|\Phi_j\rangle$ of the static Hamiltonian \hat{H}_0 , the state $|\Psi[\mathcal{E}]\rangle$ is expressed as a linear combination

$$|\Psi[\mathcal{E}]\rangle = \sum_j c_j(\mathcal{E}) |\Phi_j\rangle; \quad c_j(\mathcal{E}) = \langle\Phi_j|\Psi[\mathcal{E}]\rangle. \quad (5)$$

Using the resolution-of-the-identity $\sum_j |\Phi_j\rangle \langle\Phi_j| = \hat{1}$, the non-perturbative electric dipole response to the probe pulse $P_u[\mathcal{E}, \mathcal{F}](t) = \langle\Psi(t)|\hat{P}_u|\Psi(t)\rangle$ can be written in the frequency domain as

$$P_u[\mathcal{E}, \mathcal{F}](\omega) = i \sum_{jkmn} c_j^*(\mathcal{E}) c_n(\mathcal{E}) e^{i\omega_{jn}\tau} \frac{(e^{iQ_v})_{jk} P_{u,km} (e^{-iQ_v})_{mn}}{\omega_{km} + \omega + i\Gamma}, \quad (6)$$

where $\omega_{jk} \equiv \epsilon_j - \epsilon_k$ is the difference between the energies of the stationary states, for an operator \hat{A} , $A_{jk} \equiv \langle\Phi_j|\hat{A}|\Phi_k\rangle$ is its matrix element, $P_u(\omega) = \int_{T+\tau}^{\infty} P_u(t) e^{(i\omega - \Gamma)(t - T - \tau)} dt$ and a damping parameter Γ is introduced to regularize the Fourier integral over oscillating functions and facilitate its practical evaluation in simulations with a finite time length. Using the expansion $e^{-iQ_v} \equiv e^{i\mathcal{F}_0 P_v} = \mathbb{I} + i\mathcal{F}_0 P_v + \dots$ in Eq. (6) allows us to understand the most dominant effects on the resulting spectra, *i.e.* those that appear even in the weak probe field limit. After rearranging the summation indices, we obtain the first terms

$$P_u^{(0)}[\mathcal{E}, \mathcal{F}](\omega) = i \sum_{jk} c_j(\mathcal{E}) c_k^*(\mathcal{E}) e^{-i\omega_{jk}\tau} \frac{P_{u,kj}}{\omega - \omega_{jk} + i\Gamma}, \quad (7)$$

and

$$\frac{P_u^{(1)}[\mathcal{E}, \mathcal{F}](\omega)}{\mathcal{F}_0} = \sum_{jkm} c_j(\mathcal{E}) c_k^*(\mathcal{E}) e^{-i\omega_{jk}\tau} \frac{P_{v,km} P_{u,mj}}{\omega - \omega_{jm} + i\Gamma} + \text{c.c.}(\omega \rightarrow -\omega), \quad (8)$$

where $\text{c.c.}(\omega \rightarrow -\omega)$ labels the complex conjugation while flipping the sign of the frequency. We note, that in the relativistic theory presented here, the stationary wave functions are complex in general. As a consequence, the matrix elements $P_{v,km}$ can no longer be assumed to be real. Expressions in Eqs. (7) and (8) are in contrast with the equilibrium response theory where a response function is defined in terms of a specific eigenstate of \hat{H}_0 , *e.g.*

$|\Psi[\mathcal{E}]\rangle \equiv |\Phi_0\rangle$, and $c_j(\mathcal{E}) \equiv \delta_{j0}$ — assuming this would yield the equilibrium response functions.

The process of electronic absorption, that is of interest here, is associated with the imaginary part of the electric dipole–electric dipole response function in the frequency domain $(\chi_{\hat{P}_u, \hat{P}_v}[\mathcal{E}](\omega, T + \tau) \equiv P_u^{(1)}[\mathcal{E}, \mathcal{F}](\omega)/\mathcal{F}_0)$.⁷⁵ The resulting expression for the response function was presented by other authors,⁷⁶ while assuming that the eigenstates $|\Phi_j\rangle$, and hence the matrix elements $P_{v,km}$, are real-valued. However, this is not the case in the relativistic theory, and we here proceed by deriving the relativistic extension for the response function without making this assumption. Let ϕ_j denote the phase of the complex amplitudes c_j , *i.e.* $c_j = |c_j|e^{i\phi_j}$. By defining $\Theta_{jk}(\tau) \equiv \phi_j - \phi_k - \omega_{jk}\tau$ and using $1/(\omega + i\Gamma) = \mathcal{R}(\omega) - i\mathcal{L}(\omega)$, where \mathcal{L} and \mathcal{R} represent Lorentzian and Rayleigh lineshape functions, respectively, we can rearrange the terms in Eq. (8) and extract the imaginary part as

$$\begin{aligned} \Im \chi_{\hat{P}_u, \hat{P}_v}[\mathcal{E}](\omega, T + \tau) &= \sum_{jkm} |c_j(\mathcal{E})c_k(\mathcal{E})| \Re(P_{v,km}P_{u,mj}) \\ &\quad \times [\sin \Theta_{jk}(\tau) \mathcal{R}(\omega - \omega_{jm}) - \cos \Theta_{jk}(\tau) \mathcal{L}(\omega - \omega_{jm}) \\ &\quad + \sin \Theta_{jk}(\tau) \mathcal{R}(\omega + \omega_{jm}) + \cos \Theta_{jk}(\tau) \mathcal{L}(\omega + \omega_{jm})] \\ &\quad + \sum_{jkm} |c_j(\mathcal{E})c_k(\mathcal{E})| \Im(P_{v,km}P_{u,mj}) \\ &\quad \times [\cos \Theta_{jk}(\tau) \mathcal{R}(\omega - \omega_{jm}) + \sin \Theta_{jk}(\tau) \mathcal{L}(\omega - \omega_{jm}) \\ &\quad + \cos \Theta_{jk}(\tau) \mathcal{R}(\omega + \omega_{jm}) - \sin \Theta_{jk}(\tau) \mathcal{L}(\omega + \omega_{jm})]. \end{aligned} \quad (9)$$

The first part of this expression proportional to the real part $\Re(P_{v,km}P_{u,mj})$ coincides with the result of Walkenhorst *et al.*⁷⁶ for $P_{v,km} \in \mathbb{R}$. The second part is nonzero only for theories that lead to complex stationary states (*e.g.* when the Hamiltonian \hat{H}_0 is not real-valued), such as the relativistic theory with SO effects included. We note here, that this distinction between the theories based on complex and real orbitals is a unique feature of the non-equilibrium response function, and the differences between the formulations vanish when the

non-stationary state $|\Psi[\mathcal{E}]\rangle$ is replaced with a single eigenstate (for spatially isotropic values $\Im\chi_{\hat{p}_u, \hat{p}_u}$). Finally, we mention that the diagonal terms $j = k$ in the sums in Eq. (9) can be isolated to study separately the time delay-independent contribution and interference term that depends on the time delay τ . The interference term is a signature of the non-stationary state, leading to the spectral dependence on τ . Θ_{jk} combines the real and imaginary part of the response function and interchanges the \mathcal{L} to \mathcal{R} lineshapes, and vice-versa. The imprints of Eq. (9) can be directly connected to the simulated spectral observations and are discussed later.^{73,76}

Instead of using the non-equilibrium response theory to obtain TAS spectra, we work directly in time domain and evolve a molecular system of interest by the Liouville–von Neumann equation-of-motion (EOM). For Kohn–Sham TDDFT in an orthonormal basis, EOM takes the form

$$i\frac{\partial \mathbf{D}(t)}{\partial t} = [\mathbf{F}(t), \mathbf{D}(t)], \quad (10)$$

where $\mathbf{D}(t)$ is the time-dependent reduced one-electron density matrix describing the state of the system at time t and $\mathbf{F}(t)$ is the Fock matrix driving the time evolution and characterizing the molecular system itself as well as its interaction with the external pump–probe fields. In practice, Eq. (10) is solved numerically by propagating $\mathbf{D}(t)$ in time as detailed in Ref. 31,67, 77 and 78 as well as in Section S1.

The theoretical modelling of core-level spectroscopies is a challenging task because the spectra feature a fine structure due to scalar (SC) and spin–orbit (SO) relativistic effects.^{68,79–83} With this in mind, we have extended our recent probe-only four-component (4c) RT-TDDFT implementation^{67,68,84} to the realm of pump–probe experiments. Assuming an orthonormalized atomic orbital (AO) basis, the 4c Fock operator suitable for TAS

has the following matrix form

$$\begin{aligned}
F_{\mu\nu}^{4c}(t) = F_{\mu\nu}^{4c}[\boldsymbol{\mathcal{E}}, \boldsymbol{\mathcal{F}}](t) = & h_{\mu\nu}^{4c} - \sum_{u \in x, y, z} P_{u, \mu\nu}^{4c} \mathcal{E}_u(t) - \sum_{u \in x, y, z} P_{u, \mu\nu}^{4c} \mathcal{F}_u(t) \\
& + \sum_{\kappa\lambda} G_{\mu\nu, \kappa\lambda}^{4c} D_{\lambda\kappa}^{4c}(t, \boldsymbol{\mathcal{E}}, \boldsymbol{\mathcal{F}}) + \sum_{u \in 0-3} \int v_u^{xc} [\boldsymbol{\rho}^{4c}(\mathbf{r}, t, \boldsymbol{\mathcal{E}}, \boldsymbol{\mathcal{F}})] \Omega_{u, \mu\nu}^{4c}(\mathbf{r}) d^3\mathbf{r},
\end{aligned} \tag{11}$$

where terms on the right hand side include the one-electron Dirac operator (\mathbf{h}^{4c}), particle-field interactions via the electric dipole moment operator (\mathbf{P}_u^{4c}), two-electron (2e) Coulomb and exchange interactions, and the exchange–correlation (xc) contribution. Here, the 2e term involves the matrix of generalized anti-symmetrized electron repulsion integrals

$$G_{\mu\nu, \kappa\lambda}^{4c} = \mathcal{I}_{\mu\nu, \kappa\lambda}^{4c} - \zeta \mathcal{I}_{\mu\lambda, \kappa\nu}^{4c}; \quad \mathcal{I}_{\mu\nu, \kappa\lambda}^{4c} := \iint \Omega_{0, \mu\nu}^{4c}(\mathbf{r}_1) r_{12}^{-1} \Omega_{0, \kappa\lambda}^{4c}(\mathbf{r}_2) d^3\mathbf{r}_1 d^3\mathbf{r}_2, \tag{12}$$

with a scalar scaling factor ζ for exchange interaction, whereas the xc term requires a non-collinear xc potential v_u^{xc} , given within a generalized gradient approximation (GGA) by derivatives of the nonrelativistic xc energy density (ε^{xc}) with respect to the 4c electronic charge density (ρ_0^{4c}), spin densities (ρ_{1-3}^{4c}), as well as their gradients:

$$v_u^{xc}[\boldsymbol{\rho}^{4c}] = \frac{\partial \varepsilon^{xc}}{\partial \rho_u^{4c}} - \left(\boldsymbol{\nabla} \cdot \frac{\partial \varepsilon^{xc}}{\partial \boldsymbol{\nabla} \rho_u^{4c}} \right), \quad \rho_u^{4c} := \rho_u^{4c}(\mathbf{r}, t, \boldsymbol{\mathcal{E}}, \boldsymbol{\mathcal{F}}) = \sum_{\mu\nu} \Omega_{u, \mu\nu}^{4c}(\mathbf{r}) D_{\nu\mu}^{4c}(t, \boldsymbol{\mathcal{E}}, \boldsymbol{\mathcal{F}}). \tag{13}$$

More details about our noncollinear extension of nonrelativistic xc potentials are available in Ref. 85. In Eqs. (12) and (13), $\boldsymbol{\Omega}_u^{4c}$ stands for the matrix of overlap distribution functions⁸⁴

$$\Omega_{u, \mu\nu}^{4c}(\mathbf{r}) = \mathbf{X}_\mu^\dagger(\mathbf{r}) \boldsymbol{\Sigma}_u \mathbf{X}_\nu(\mathbf{r}), \quad \boldsymbol{\Sigma}_u = \begin{pmatrix} \boldsymbol{\sigma}_u & \mathbf{0}_2 \\ \mathbf{0}_2 & \boldsymbol{\sigma}_u \end{pmatrix}, \tag{14}$$

defined as the product of *orthonormal* 4c AO basis functions $\mathbf{X}_\mu(\mathbf{r}) := \mathbf{X}_\mu^{\text{RKB}}(\mathbf{r})$ fulfilling a restricted kinetic balance (RKB) condition in their small-component,⁸⁶ and 4c operators

associated with the electronic charge density (Σ_0) and spin densities (Σ_{1-3}). The latter ones are defined via the 2×2 zero matrix ($\mathbf{0}_2$), identity matrix (σ_0), and Pauli spin matrices ($\sigma_1, \sigma_2, \sigma_3$). Note that prior to their use in Eq. (10), both Fock and density matrix are transformed into the basis of ground-state molecular orbitals, obtained from the solution of self-consistent field equations.

While simulation of XAS by means of full 4c RT-TDDFT method is nowadays feasible but computationally challenging,⁶⁸ its further extension towards pump-probe experiments poses additional computational burden. Therefore, there is interest in developing approximate relativistic methods enabling RT calculations in two-component (2c) regime while maintaining the accuracy of the parent 4c approach. Hence, alongside of the 4c method that serves as a gold-standard reference, we put-forth a first formulation and implementation of an atomic mean-field exact two-component Hamiltonian (amfX2C) within the realm of RT-TDDFT and apply it to simulate (X)TAS spectra. As proven for self-consistent field calculations, the simple yet numerically accurate amfX2C approach accounts for so-called SC and SO two-electron (2e) and exchange-correlation (xc) picture-change (PC) effects that arise from the X2C transformation, in contrast to the commonly used one-electron X2C (1eX2C) Hamiltonian.⁶⁴ Furthermore, as demonstrated on simple XAS spectra of transition metal and actinide compounds, the absence of these PC effects in 1eX2C results in a substantial overestimation of L- and M-edge SO splittings, whereas the amfX2C Hamiltonian reproduces all essential spectral features such as shape, position and SO splitting in excellent agreement with 4c references, while offering more than 7-fold speed-up.⁷² A similar acceleration was reported previously on RT-TDDFT based on 1eX2C.⁵⁴

The central idea of our RT-TDDFT amfX2C approach is the matrix transformation of the original 4c EOM in Eq. (10) to its diagonally-dominant form using a static (time-independent) unitary matrix \mathbf{U} . By maintaining only the large-component-large-component

(LL) block of the transformed 4c EOM, one arrives at the 2c EOM^{54,72}

$$i \frac{\partial \tilde{\mathbf{D}}^{2c}(t)}{\partial t} = [\tilde{\mathbf{F}}^{2c}(t), \tilde{\mathbf{D}}^{2c}(t)] \quad (15)$$

with so-called 2c PC transformed Fock and density matrix

$$\tilde{F}_{\mu\nu}^{2c}(t) = \left[\mathbf{U}^\dagger \mathbf{F}^{4c}(t) \mathbf{U} \right]_{\mu\nu}^{\text{LL}}, \quad \tilde{D}_{\mu\nu}^{2c}(t) = \left[\mathbf{U}^\dagger \mathbf{D}^{4c}(t) \mathbf{U} \right]_{\mu\nu}^{\text{LL}}. \quad (16)$$

In consistency with our previous works we use notation with tildes to indicate picture-change transformed quantities.^{64,72} Of significant importance is the observation that the *correctly* transformed 2c Fock matrix involves not only the PC transformed density matrix ($\tilde{\mathbf{D}}^{2c}$), but also overlap distribution matrix, as well as one- and two-electron integrals.^{64,72} In connection to Eq. (11), our 2c RT-TDDFT (X)TAS reads

$$\begin{aligned} \tilde{F}_{\mu\nu}^{2c}(t) = \tilde{F}_{\mu\nu}^{2c}[\boldsymbol{\mathcal{E}}, \boldsymbol{\mathcal{F}}](t) = & \tilde{h}_{\mu\nu}^{2c} - \sum_{u \in x,y,z} \tilde{P}_{u,\mu\nu}^{2c} \mathcal{E}_u(t) - \sum_{u \in x,y,z} \tilde{P}_{u,\mu\nu}^{2c} \mathcal{F}_u(t) \\ & + \sum_{\kappa\lambda} \tilde{G}_{\mu\nu,\kappa\lambda}^{2c} \tilde{D}_{\lambda\kappa}^{2c}(t, \boldsymbol{\mathcal{E}}, \boldsymbol{\mathcal{F}}) + \sum_{u \in 0-3} \int v_u^{xc} [\tilde{\rho}^{2c}(\mathbf{r}, t, \boldsymbol{\mathcal{E}}, \boldsymbol{\mathcal{F}})] \tilde{\Omega}_{u,\mu\nu}^{2c}(\mathbf{r}) d^3\mathbf{r}. \end{aligned} \quad (17)$$

Note however, that the presence of picture-change transformed overlap distribution matrix ($\tilde{\Omega}^{2c}$) in both 2e and xc interaction terms makes the evaluation of $\tilde{\mathbf{F}}^{2c}$ computationally more demanding than the original 4c Fock matrix. Therefore, in line with the amfX2C approach introduced originally for the static (time-independent) SCF case⁶⁴ and extended later to the response theory formalism involving electric field(s),⁷² $\tilde{\mathbf{F}}^{2c}$ in Eq. (17) can be approximated by a computationally efficient form built with untransformed (without the tilde) overlap

distributions (Ω^{2c}), i.e.,

$$\begin{aligned} \tilde{F}_{\mu\nu}^{2c}(t) \approx F_{\mu\nu}^{\text{amfX2C}}[\mathcal{E}, \mathcal{F}](t) = & \tilde{h}_{\mu\nu}^{2c} - \sum_{u \in x,y,z} \tilde{P}_{u,\mu\nu}^{2c} \mathcal{E}_u(t) - \sum_{u \in x,y,z} \tilde{P}_{u,\mu\nu}^{2c} \mathcal{F}_u(t) + \Delta \tilde{F}_{\oplus,\mu\nu}^{\text{amfX2C}} \\ & + \sum_{\kappa\lambda} G_{\mu\nu,\kappa\lambda}^{2c} \tilde{D}_{\lambda\kappa}^{2c}(t, \mathcal{E}, \mathcal{F}) + \sum_{u \in 0-3} \int v_u^{xc} [\rho^{2c}(\mathbf{r}, t, \mathcal{E}, \mathcal{F})] \Omega_{u,\mu\nu}^{2c}(\mathbf{r}) d^3\mathbf{r}. \end{aligned} \quad (18)$$

In fact, Eq. (18) defines our 2c amfX2C Fock matrix applied in actual RT (X)TAS simulations. Here, the picture-change corrections, defined as the difference between transformed and untransformed 2e and xc interaction terms, are taken into account approximately via $\Delta \tilde{\mathbf{F}}_{\oplus}^{\text{amfX2C}}$ and given by a superposition of corresponding *static* atomic quantities:^{64,72}

$$\Delta \tilde{\mathbf{F}}_{\oplus}^{\text{amfX2C}} = \bigoplus_{K=1}^M \Delta \tilde{\mathbf{F}}_K^{2c,2e} + \Delta \tilde{\mathbf{F}}_K^{2c,xc}, \quad (19)$$

where

$$\Delta \tilde{\mathbf{F}}_K^{2c,2e} = (\tilde{\mathbf{G}}_K^{2c} - \mathbf{G}_K^{2c}) \tilde{\mathbf{D}}_K^{2c} \quad (20)$$

$$\Delta \tilde{\mathbf{F}}_K^{2c,xc} = \sum_{u \in 0-3} \int v_u^{xc} [\tilde{\rho}_K^{2c}(\mathbf{r})] \tilde{\Omega}_u^{2c}(\mathbf{r}) d^3\mathbf{r} - \sum_{u \in 0-3} \int v_u^{xc} [\rho^{2c}(\mathbf{r})] \Omega_u^{2c}(\mathbf{r}) d^3\mathbf{r}. \quad (21)$$

Here, K runs over all atoms in an M -atomic system and labels atomic quantities obtained from independent atomic SCF calculations, each performed in the orthonormal AO basis of K th atom. While a theoretical justification enabling us to build $\Delta \tilde{\mathbf{F}}_{\oplus}^{\text{amfX2C}}$ from static (time-independent) quantities is available in Ref. 72, a pseudo-code highlighting the essential steps for evaluating $\Delta \tilde{\mathbf{F}}_{\oplus}^{\text{amfX2C}}$ is presented in Ref. 64.

The final TAS spectra are obtained within the RT-TDDFT framework from the differential induced dipole moment

$$\Delta \mu_{uv}^{\text{TAS}}(t) = \text{Tr} \{ \mathbf{P}_u [\mathbf{D}_v^{\text{pp}}(t) - \mathbf{D}_v^{\text{p}}(t)] \} \equiv \mu_{uv}^{\text{ind,pp}}(t) - \mu_{uv}^{\text{ind,p}}(t), \quad u, v \in \{x, y, z\}, \quad (22)$$

where $\mu_{uv}^{\text{ind}}(t)$ denotes the expectation value of the dipole operator. The computation of TAS spectra involves performing two simulations for recording the dipole moment at each time step; these simulations and their quantities are denoted by p and pp subscripts, indicating that the real-time propagation used pump-only pulse and pump together with the probe pulse, respectively. This difference is calculated to isolate the effect of the probe pulse on the non-stationary electronic wavepacket, *i.e.* to eliminate pump-only-dependent terms in Eq. (7). This procedure is in contrast with the simulations initiated from an equilibrium stationary state (*i.e.* without pump), for which Eq. (7) simplifies to the static dipole moment that is subtracted in Eq. (22), and the absorption spectra thus only require one time propagation simulation. The differential dipole moment is subsequently transformed into the frequency domain (like in Eq. (6)). Finally, the TAS spectral function $S^{\text{TAS}}(\omega)$ is evaluated analogously to its ground state absorption counterpart as,

$$S^{\text{TAS}}(\omega) = \frac{4\pi\omega}{3c} \Im \text{Tr}[\boldsymbol{\alpha}^{\text{TAS}}(\omega)] \quad \text{where,} \quad \alpha_{uv}^{\text{TAS}} = \frac{\Delta\mu_{uv}^{\text{TAS}}(\omega)}{\mathcal{F}_0} . \quad (23)$$

In Eq. (23), c is the speed of light, Tr is a trace over Cartesian components of the polarizability tensor $\boldsymbol{\alpha}$.

In simulated X-ray spectra, signals originating from transitions between valence and high-lying virtual orbitals can appear. These are non-physical in calculations using finite atom-centered basis sets, since above-ionization states are ill-described in such cases. To eliminate these spurious peaks, we restrict the probe operator to act only on a selected subset of core and virtual orbitals by zeroing all other elements of the dipole matrix when applying the probe pulse thus making the non-physical transitions artificially dipole-forbidden. This technique, called selective perturbation, was introduced in our previous works in the context of XAS calculations using both RT-TDDFT⁶⁸ as well as damped linear response TDDFT.⁸³ Note that no restriction is applied on the pump pulse as that is purposefully tuned to an excitation from valence to low-lying orbitals.

In line with the spectral analysis technique for RT-TDDFT simulations presented in Ref. 67, we assign the nature of electronic excitations underlying a particular TAS resonance feature by a dipole-weighted transition matrix analysis (DWTA). For a resonant frequency ω' , the Fourier component $\mathcal{T}(\omega')$ of the time-domain signal $\mathcal{T}(t)$ contains all information.

$$\mathcal{T}(\omega') = \int_0^\infty \mathcal{T}(t + T + \tau) e^{(i\omega' - \Gamma)t} dt ; \quad \mathcal{T}_{uv;ai}(t) = \Delta\mu_{uv;ai}^{\text{TAS}}(t) = \mu_{uv;ai}^{\text{ind,pp}}(t) - \mu_{uv;ai}^{\text{ind,p}}(t) . \quad (24)$$

Here, a, i runs over occupied and virtual spinors, respectively, and we accounted for the fact that only the time signal after the probe pulse is used for the Fourier transform. We use the differential induced dipole moment (Eq (22)) at a specific resonance frequency (ω'), to obtain the contribution of individual occupied-virtual pairs towards the spectral peak. $\mathcal{T}(t)$ matrix is obtained by averaging over the Cartesian components.

The above formulated RT-TDDFT methodology was implemented in the RESPECT program,⁸⁴ and used to investigate the TAS spectra of two prototypical molecules, ethylene and thiophene at the valence and core ($L_{2,3}$) energy region, respectively, employing 1c non-relativistic, 2c amfX2C and 4c Dirac-Coulomb Hamiltonian. Geometries of the systems are given in SI. Uncontracted aug-cc-pVXZ basis set (X=T(C), D(H) for ethylene and T(S), D(C,H) for thiophene)⁸⁷⁻⁹⁰ with PBE0-40HF hybrid xc functional⁹¹ including 40% exact exchange contributions is used.⁸³ For all nuclei, a finite-sized Gaussian model was used. For core absorption processes, we use the selective perturbation scheme described above, whereby only electric dipole moment contributions originating from the core S $2p_{1/2}$ and $2p_{3/2}$ orbitals are considered to be dipole-allowed.⁶⁸ The details of the TAS computational setup are elucidated in Table 1 and Figure S1. Note that the choice of direction of polarization of pump pulse (\mathbf{n}) is important as the spectra are sensitive to geometrical features.

For ethylene, we study the effect of the degrees of freedom specific to pump-probe processes, focusing on pump pulse strength and pump-probe time delay. Firstly, the effect of pump pulse strength on the TAS spectra is shown in Figure 1. The electronic wavepacket

Table 1: Computational setup: The pump and probe pulse parameters corresponds to Eq. (1) and (2). Carrier frequency (ω_0) is tuned to the first bright excited state along the direction of dipole-allowed transition (n). Time duration (T) of the pump pulse corresponds to 15 carrier periods. The pump pulse amplitude (\mathcal{E}_0) is chosen to sufficiently depopulate the ground state. A weak δ probe of amplitude \mathcal{F}_0 along all the Cartesian components are applied. The probed system is evolved for n_{step} with Δt_{step} length as detailed in Section S1, using the convergence criterion for micro-iterations $|\mathbf{D}^{(n)}(t + \Delta t) - \mathbf{D}^{(n+1)}(t + \Delta t)| < 10^{-6}$. These parameters are used unless otherwise stated.

Molecule	$\mathcal{E}(t)$				$\mathcal{F}(t)$		RT simulation	
	ω_0 (au)	T (au)	n	\mathcal{E}_0 (au)	\mathcal{F}_0 (au)		n_{step}	Δt_{step} (au)
C ₂ H ₄	0.2762	341.10	x	0.01	0.01		20000	0.15
C ₄ H ₄ S	0.2135	441.20	y	0.05	0.01		25000	0.20

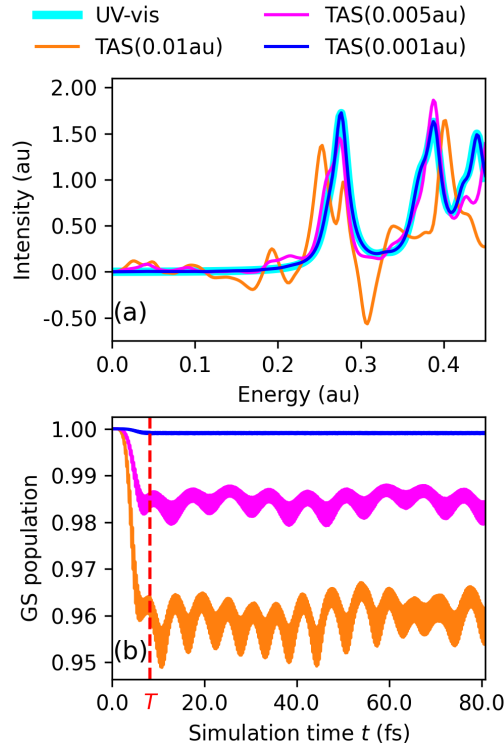


Figure 1: Ethylene – (a) Comparison of UV-vis and TAS spectra with varying \mathcal{E}_0 , given in parentheses, obtained with amfX2C Hamiltonian. TAS is computed at $\tau = 0.0$ with a damping parameter $\Gamma = 0.01$ au. (b) Variation in the ground state population as a function of simulation time t obtained as $\text{Tr}[\mathbf{D}(0)\mathbf{D}(t)]$, with pump amplitudes as color coded in (a). T (in red) marks the duration of pump pulse.

$|\Psi[\mathcal{E}]\rangle$ generated by the pump pulse comprises of an admixture of ground and excited electronic states (see Eq. (5)), with the effective depopulation of ground state being proportional

to \mathcal{E}_0 . The ground state occupancy at time t is estimated as $\text{Tr}[\mathbf{D}(0)\mathbf{D}(t)]$.⁷⁶ It is evident from Figure 1, that considerable depopulation of ground state is necessary to differentiate TAS spectra from ordinary ground state absorption spectra. The negative intensity signal at about 0.3 au and $\mathcal{E}_0 = 0.01$ au in Figure 1a is a hallmark of non-stationary state involved in this pump-probe process and is a consequence of mixing Lorentzian and Rayleigh lineshape functions as derived in Eq. (9). TAS spectra of ethylene obtained with $\mathcal{E}_0 = 0.01$ au is in a good agreement with the pioneering work by Giovannini et al.³⁴ using Octopus code.^{92–94} However, due to different computational setup and lack of experimental references we do not focus on a detailed assignment of the TAS spectral features. For exact theory, the ground state population at $t > T + \tau$ depends only on τ and pulse intensities, and is constant with respect to the simulation time t . This can be derived from Eqs. (4) and (5) as,

$$\begin{aligned}
|c_0(\mathcal{E})|^2 &= |\langle \Phi_0 | \Psi(t) \rangle|^2 \\
&= |\langle \Phi_0 | e^{-i\hat{H}_0(t-T-\tau)} e^{-i\hat{Q}_v} e^{-i\hat{H}_0\tau} | \Psi[\mathcal{E}] \rangle|^2 \\
&= |\langle \Phi_0 | e^{-i\hat{Q}_v} e^{-i\hat{H}_0\tau} | \Psi[\mathcal{E}] \rangle|^2 .
\end{aligned} \tag{25}$$

However, this behaviour does not hold for approximate mean-field methods such as HF or DFT, where the exponential term $e^{-i\hat{H}_0(t-T-\tau)}$ does not drop out of the integration as a consequence of the implicit time dependence incorporated in the Fock matrix. The resulting oscillations in the ground state population, as seen in Figure 1b, are artefacts attributed to the use of adiabatic approximation.^{95–97}

From an experimental point-of-view, the most important degree of freedom in TAS is the pump–probe time delay τ . The influence of τ on TAS for ethylene is depicted in Figure 2c. As the pump pulse is tuned to the first bright state in the ground state absorption spectrum (**A'** in Figure 2b), this ground state peak is split into peaks **A**, **B** and **C** in the TAS. DWTA analysis of **A'**, **A**, **B** and **C** (shown in Figure 2d, S3 and S4) shares same dominantly contributing transition of $\pi \rightarrow \pi^*$ character involving degenerate spinor pair (15,16) \rightarrow

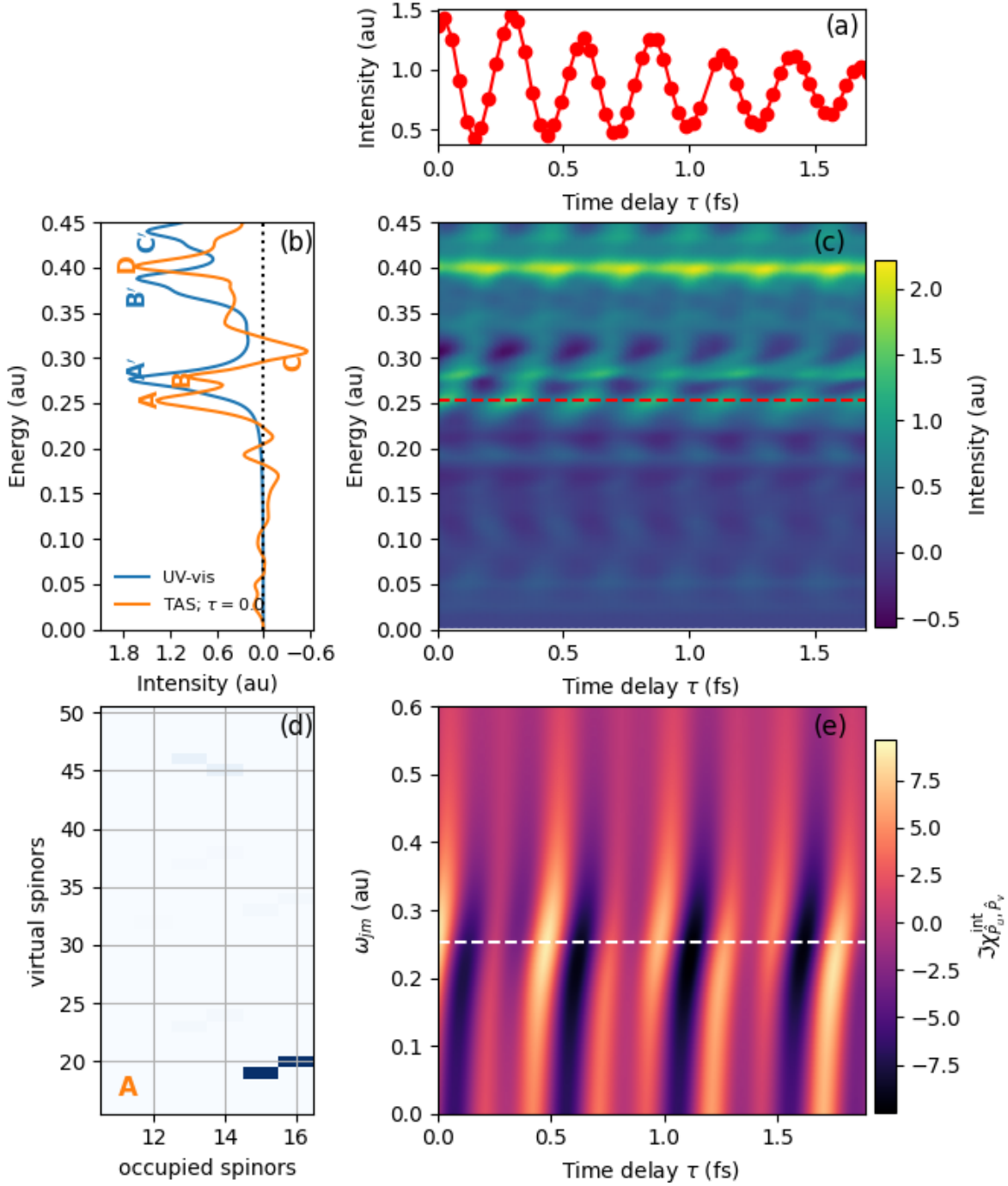


Figure 2: Ethylene – (a) Variation in intensity with τ for the TAS spectral peak at $\omega_0 = 0.2534$ au; (b) Ground state absorption and TAS spectra at $\tau = 0.0$; (c) TAS spectra with varying τ ; (d) DWTA of the TAS peak **A** at $\omega_0 = 0.2534$ au and $\tau = 0.0$. The intensity of blue color corresponds to the intensity of the particular excitation; (e) $\Im \chi_{\hat{p}_u, \hat{p}_v}^{\text{int}}[\mathcal{E}](0.2534, 341.10 + \tau)$ is given in Eq. (26), for degenerate k, j spinor-pair selected as $(15,16) \rightarrow (19,20)$ and $(13,14) \rightarrow (46,45)$ with orbital energy difference of 0.3305 au and 0.6039 au, respectively. White dashed lines corresponds to the resonant ω . 2c amfX2C Hamiltonian is used for the RT simulation.

(19,20). Secondary contributions come from transitions involving degenerate spinor pair (13,14)→(46,45). Interestingly, peak **D** has completely different character from any of the features obtained in the ground state absorption spectra, further emphasising on the novelty of this spectroscopic technique to probe states (and therein molecular orbitals) not directly accessible by purely ground or excited-state absorption.

A striking feature of the TAS spectrum in Figure 2 is the oscillation of spectral intensity with τ . As shown in Figure S5, this feature is not associated with the variation of the contributing orbitals underlying a particular frequency peak with time-delay. Therefore, non-equilibrium response theory was applied to understand qualitatively the origin of these modulations. Considering that the system consists of only light elements (C,H), a reasonable approach is to use only the non-relativistic component associated with the real part of the response function in Eq. (9). As shown in Figure 2d, the DWTA of peak **A** reveals that only two transitions [(15, 16) → (19, 20)] and [(13, 14) → (46, 45)] with orbital energy difference of 0.3305 au and 0.6039 au contribute. Therefore, only these transitions appear in the summation over k, j in Eq. (9). By discretizing the summation over m such that ω_{jm} is within the frequency range [0.0, 0.6au], and further assuming that the two transitions: (I) are of equal probability, i.e. $|c_j(\mathcal{E})c_k(\mathcal{E})| = 1$; (II) have zero phase-factor difference ($\phi_j - \phi_k = 0$); (III) have the same electric dipole transition moments for all m ($P_{v,km} = 1$), we arrive at a simplified formula for the response function, plotted in Figure 2e,

$$\begin{aligned} \Im \chi_{\hat{P}_u, \hat{P}_v}^{\text{int}}[\mathcal{E}](0.2534, 341.10 + \tau) = & \sum_{\omega_{kj} \in 0.3305, 0.6039} \cos(-\omega_{kj}\tau) \left\{ \mathcal{L}(0.2534 - \omega_{jm}) - \mathcal{L}(0.2534 + \omega_{jm}) \right\} \\ & + \sin(-\omega_{kj}\tau) \left\{ \mathcal{R}(0.2534 - \omega_{jm}) + \mathcal{R}(0.2534 + \omega_{jm}) \right\}. \quad (26) \end{aligned}$$

Even with such simplifications, we were able to mimic the appearance of the intensity oscillation with τ , unique to TAS. Especially we are capable of capturing the decrease in intensity at the maxima at $\omega = 0.2534$ au, marked by white dashed line in Figure 2e. Providing more information about initial phase difference and dipole contributions, will enable one to more

closely reproduce the spectral feature from response theory.

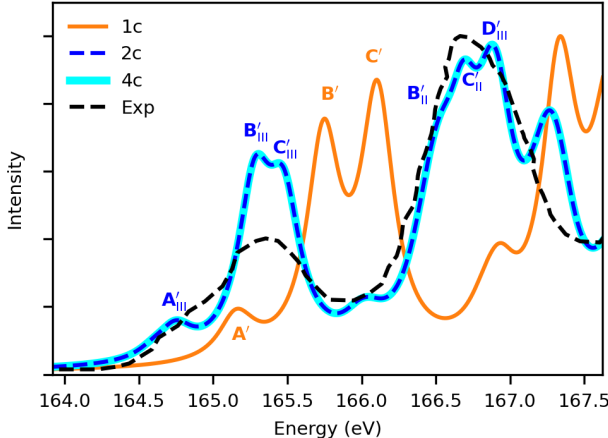


Figure 3: Thiophene – Ground state $L_{2,3}$ -edge X-ray absorption spectra obtained with 1c non-relativistic (*orange*), 2c amfX2C (*blue*) and 4c Dirac–Coulomb (*cyan*) Hamiltonian using a damping factor of $\Gamma = 0.005$ au. The simulated spectra is shifted by +1.42 eV, to match the first experimental peak. Experimental results are digitized from Ref. 98. DWTA analysis of the spectral peaks obtained with 1c and 2c Hamiltonians are shown in Figures S6 and S7, respectively.

Next, we focus on the energy region of the core $L_{2,3}$ -edge of sulphur in thiophene. The experimental⁹⁸ and simulated ground state XAS at the non-relativistic (1c), amfX2C (2c), and Dirac–Coulomb (4c) Hamiltonian level are presented in Figure 3, clearly demonstrating the importance of including SO coupling effects to reproduce the doublet structure of the spectra (B'_{III} , C'_{III} versus B'_{II} , C'_{II}). The DWTA analysis of individual peaks (shown in Figure S6 and S7) reveals that the lower energy feature corresponds to promotion from the S $2p_{3/2}$, whereas the higher energy ones are from S $2p_{1/2}$. Each of the SO split band, is further split due to the molecular field (MF), corresponding to $9e_{1/2}$, $8e_{1/2}$ (L_3 component) and $7e_{1/2}$ (L_2 component) molecular orbitals and leading to the lower energy separated doublets. The MF doublet (B' and C') also appears at the 1c level. The SO split counterpart A'_{II} of band A'_{III} is hidden under the more intense B'_{III} and C'_{III} doublet. The experimental SO splitting of 1.2 eV is well reproduced by our relativistic Hamiltonian. We would like to draw the attention of the readers to the remarkable agreement between the XAS obtained with our amfX2C and gold-standard Dirac–Coulomb Hamiltonian, the former being generated at

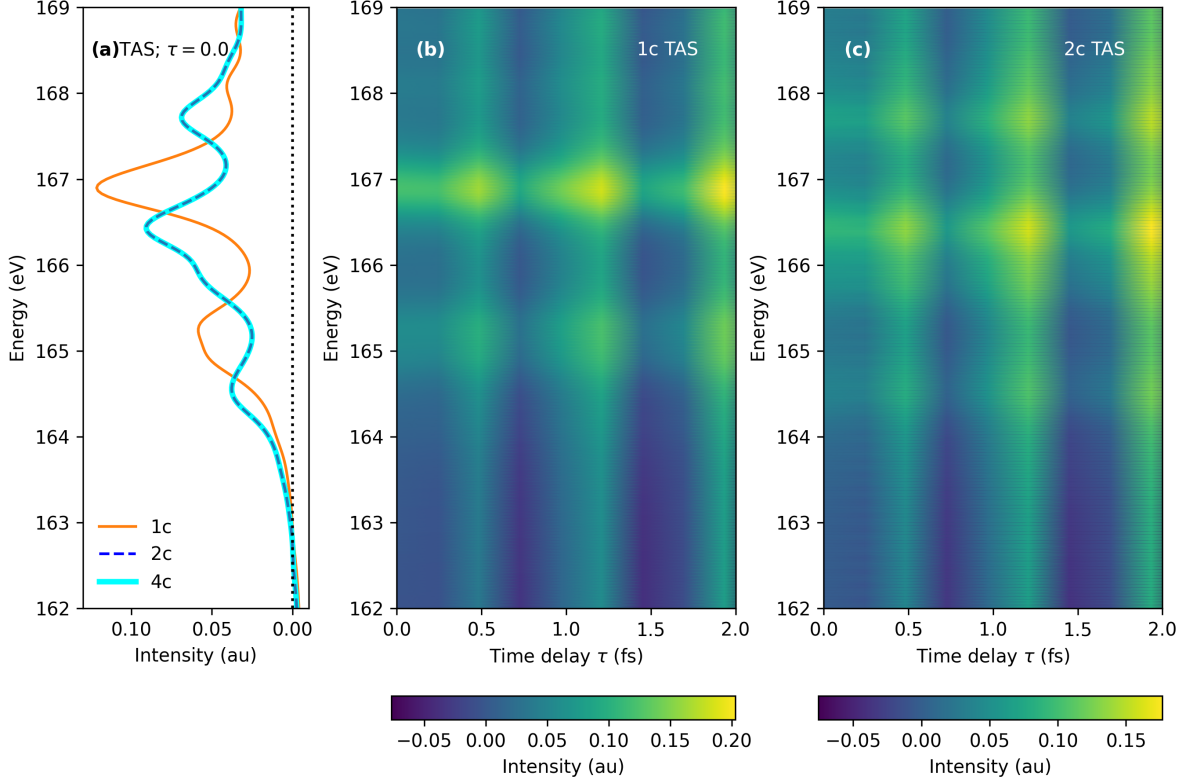


Figure 4: Thiophene – (a) TAS at $\tau = 0$ with 1c non-relativistic (*orange*), 2c amfX2C (*blue*) and 4c Dirac–Coulomb (*cyan*) Hamiltonian; (b) Variation in TAS spectra with τ obtained with 1c non-relativistic Hamiltonian; (c) Variation in TAS spectra with τ obtained with 2c amfX2C Hamiltonian. All spectra are obtained with a damping factor $\Gamma = 0.01$ au.

less than 1/7th of the computational cost of the later. In addition, all other computational characteristics of RT simulations such as number of micro-iterations and convergence pattern remain identical for 2c and 4c regime. Finally, we compute the TAS spectra using a setup described in Table 1 and shown in Figure 4. The importance of incorporating relativistic effects is further reinforced here as evident from the SO split doublet spectral peaks generated using the relativistic Hamiltonian, as seen by comparing Figure 4b and 4c. Again, the resemblance of the TAS simulated at the 2c and 4c level at $\tau = 0.0$ (in Figure 4a) further gives us confidence to use the modern amfX2C Hamiltonian for larger systems in future studies.

In summary, we have formulated and implemented a theoretical approach for first-principle simulation of TAS spectra based on relativistic RT-TDDFT frameworks, consis-

tently applicable across the Periodic Table and element-specific core energy regions. Alongside gold-standard four-component methodology, remarkable accuracy and significant computational acceleration was achieved by introducing amfX2C Hamiltonian within RT-TDDFT framework. With this, we identify and interpret the unique features associated with TAS spectra, notably the appearance of negative intensity peaks and oscillations in intensity of a particular energy feature with pump-probe time delay. These observations were further supported by non-equilibrium response theory, relativistic generalization of which was also formulated in this letter. Finally, we showcase fingerprints of spin-orbit effects on the X(T)AS spectra near the sulphur $L_{2,3}$ -edge of thiophene. We believe, this work constitutes a significant methodological advancement for studying and interpreting transient absorption spectra, applicable to X-ray regimes and/or heavy systems. Work along this direction is currently ongoing in our laboratory.

Acknowledgement

We acknowledge the support received from the Research Council of Norway through a Centre of Excellence Grant (No. 262695), a Research Grant (No. 315822), and Mobility Grants (No. 301864 and No. 314814), as well as the use of computational resources provided by UNINETT Sigma2 – The National Infrastructure for High Performance Computing and Data Storage in Norway (Grant No. NN4654K). In addition, this project received funding from the European Union’s Horizon 2020 research and innovation program under the Marie Skłodowska-Curie Grant Agreement No. 945478 (SASPRO2), and the Slovak Research and Development Agency (Grant No. APVV-21-0497).

Supporting Information Available

Real-time propagator; Computational setup; Dependence of TAS on pump pulse carrier frequency; DWTAs; Molecular geometries. This information is available free of charge via the

References

- (1) Berera, R.; van Grondelle, R.; Kennis, J. T. M. Ultrafast transient absorption spectroscopy: principles and application to photosynthetic systems. *Photosyn. Res.* **2009**, *101*, 105–118.
- (2) Sommer, A. M. *Ultrafast strong field dynamics in dielectrics*; Springer International Publishing: Cham, 2016; pp 31–34.
- (3) Geneaux, R.; Marroux, H. J. B.; Guggenmos, A.; Neumark, D. M.; Leone, S. R. Transient absorption spectroscopy using high harmonic generation: a review of ultrafast X-ray dynamics in molecules and solids. *Philos. Trans. R. Soc. A* **2019**, *377*, 20170463.
- (4) Kling, M. F.; Vrakking, M. J. Attosecond electron dynamics. *Annu. Rev. Phys. Chem.* **2008**, *59*, 463–492.
- (5) Tzallas, P.; Skantzakis, E.; Nikolopoulos, L.; Tsakiris, G. D.; Charalambidis, D. Extreme-ultraviolet pump–probe studies of one-femtosecond-scale electron dynamics. *Nat. Phys.* **2011**, *7*, 781–784.
- (6) Bressler, C.; Chergui, M. Ultrafast x-ray absorption spectroscopy. *Chem. Rev.* **2004**, *104*, 1781–1812.
- (7) Loh, Z.-H.; Leone, S. R. Capturing ultrafast quantum dynamics with femtosecond and attosecond x-ray core-level absorption spectroscopy. *J. Phys. Chem. Lett.* **2013**, *4*, 292–302.
- (8) Shelby, M. L.; Lestrangle, P. J.; Jackson, N. E.; Haldrup, K.; Mara, M. W.; Stickrath, A. B.; Zhu, D.; Lemke, H. T.; Chollet, M.; Hoffman, B. M. et al. Ultrafast excited

- state relaxation of a metalloporphyrin revealed by femtosecond x-ray absorption spectroscopy. *J. Am. Chem. Soc.* **2016**, *138*, 8752–8764.
- (9) Curchod, B. F.; Martínez, T. J. Ab initio nonadiabatic quantum molecular dynamics. *Chem. Rev.* **2018**, *118*, 3305–3336.
- (10) Hentschel, M.; Kienberger, R.; Spielmann, C.; Reider, G. A.; Milosevic, N.; Brabec, T.; Corkum, P.; Heinzmann, U.; Drescher, M.; Krausz, F. Attosecond metrology. *Nature* **2001**, *414*, 509–513.
- (11) Baltuška, A.; Udem, T.; Uiberacker, M.; Hentschel, M.; Goulielmakis, E.; Gohle, C.; Holzwarth, R.; Yakovlev, V. S.; Scrinzi, A.; Hänsch, T. W. et al. Attosecond control of electronic processes by intense light fields. *Nature* **2003**, *421*, 611–615.
- (12) Kienberger, R.; Goulielmakis, E.; Uiberacker, M.; Baltuska, A.; Yakovlev, V.; Bammer, F.; Scrinzi, A.; Westerwalbesloh, T.; Kleineberg, U.; Heinzmann, U. et al. Atomic transient recorder. *Nature* **2004**, *427*, 817–821.
- (13) Diels, J.-C.; Rudolph, W. *Ultrashort laser pulse phenomena*; Elsevier, 2006.
- (14) Goulielmakis, E.; Loh, Z.-H.; Wirth, A.; Santra, R.; Rohringer, N.; Yakovlev, V. S.; Zharebtsov, S.; Pfeifer, T.; Azzeer, A. M.; Kling, M. F. et al. Real-time observation of valence electron motion. *Nature* **2010**, *466*, 739–743.
- (15) Wirth, A.; Hassan, M. T.; Grguraš, I.; Gagnon, J.; Moulet, A.; Luu, T. T.; Pabst, S.; Santra, R.; Alahmed, Z.; Azzeer, A. et al. Synthesized light transients. *Science* **2011**, *334*, 195–200.
- (16) Leone, S. R.; McCurdy, C. W.; Burgdörfer, J.; Cederbaum, L. S.; Chang, Z.; Dudovich, N.; Feist, J.; Greene, C. H.; Ivanov, M.; Kienberger, R. et al. What will it take to observe processes in "real time"? *Nat. Photonics* **2014**, *8*, 162–166.

- (17) Kraus, P. M.; Mignolet, B.; Baykusheva, D.; Rupenyan, A.; Horný, L.; Penka, E. F.; Grassi, G.; Tolstikhin, O. I.; Schneider, J.; Jensen, F. et al. Measurement and laser control of attosecond charge migration in ionized iodoacetylene. *Science* **2015**, *350*, 790–795.
- (18) Kuleff, A. I.; Kryzhevoi, N. V.; Pernpointner, M.; Cederbaum, L. S. Core ionization initiates subfemtosecond charge migration in the valence shell of molecules. *Phys. Rev. Lett.* **2016**, *117*, 093002.
- (19) Nisoli, M.; Decleva, P.; Calegari, F.; Palacios, A.; Martín, F. Attosecond electron dynamics in molecules. *Chem. Rev.* **2017**, *117*, 10760–10825.
- (20) Canova, F.; Poletto, L. *Optical technologies for extreme-ultraviolet and soft x-ray coherent sources*; Springer, 2015.
- (21) Duris, J.; Li, S.; Driver, T.; Champenois, E. G.; MacArthur, J. P.; Lutman, A. A.; Zhang, Z.; Rosenberger, P.; Aldrich, J. W.; Coffee, R. et al. Tunable isolated attosecond X-ray pulses with gigawatt peak power from a free-electron laser. *Nat. Photonics* **2020**, *14*, 30–36.
- (22) Chen, L. X.; Zhang, X. Photochemical processes revealed by x-ray transient absorption spectroscopy. *J. Phys. Chem. Lett.* **2013**, *4*, 4000–4013.
- (23) Bhattacharjee, A.; Leone, S. R. Ultrafast x-ray transient absorption spectroscopy of gas-phase photochemical reactions: A new universal probe of photoinduced molecular dynamics. *Acc. Chem. Res.* **2018**, *51*, 3203–3211.
- (24) Cavalieri, A. L.; Müller, N.; Uphues, T.; Yakovlev, V. S.; Baltuška, A.; Horvath, B.; Schmidt, B.; Blümel, L.; Holzwarth, R.; Hendel, S. et al. Attosecond spectroscopy in condensed matter. *Nature* **2007**, *449*, 1029–1032.

- (25) Schultze, M.; Ramasesha, K.; Pemmaraju, C.; Sato, S.; Whitmore, D.; Gandman, A.; Prell, J. S.; Borja, L.; Prendergast, D.; Yabana, K. et al. Attosecond band-gap dynamics in silicon. *Science* **2014**, *346*, 1348–1352.
- (26) Lucchini, M.; Sato, S. A.; Ludwig, A.; Herrmann, J.; Volkov, M.; Kasmi, L.; Shinohara, Y.; Yabana, K.; Gallmann, L.; Keller, U. Attosecond dynamical Franz-Keldysh effect in polycrystalline diamond. *Science* **2016**, *353*, 916–919.
- (27) Picón, A.; Plaja, L.; Biegert, J. Attosecond x-ray transient absorption in condensed-matter: a core-state-resolved Bloch model. *New J. Phys.* **2019**, *21*, 043029.
- (28) Yabana, K.; Bertsch, G. Time-dependent local-density approximation in real time. *Phys. Rev. B* **1996**, *54*, 4484.
- (29) Tsolakidis, A.; Sánchez-Portal, D.; Martin, R. M. Calculation of the optical response of atomic clusters using time-dependent density functional theory and local orbitals. *Phys. Rev. B* **2002**, *66*, 235416.
- (30) Isborn, C. M.; Li, X. Modeling the doubly excited state with time-dependent Hartree–Fock and density functional theories. *J. Chem. Phys.* **2008**, *129*, 204107.
- (31) Lopata, K.; Govind, N. Modeling fast electron dynamics with real-time time-dependent density functional theory: application to small molecules and chromophores. *J. Chem. Theory Comput.* **2011**, *7*, 1344–1355.
- (32) Lopata, K.; Van Kuiken, B. E.; Khalil, M.; Govind, N. Linear-response and real-time time-dependent density functional theory studies of core-level near-edge x-ray absorption. *J. Chem. Theory Comput.* **2012**, *8*, 3284–3292.
- (33) Sato, T.; Ishikawa, K. L. Time-dependent complete-active-space self-consistent-field method for multielectron dynamics in intense laser fields. *Phys. Rev. A* **2013**, *88*, 023402.

- (34) Giovannini, U. D.; Brunetto, G.; Castro, A.; Walkenhorst, J.; Rubio, A. Simulating pump-probe photoelectron and absorption spectroscopy on the attosecond timescale with time-dependent density functional theory. *Chem. Phys. Chem* **2013**, *14*, 1363–1376.
- (35) Lian, C.; Guan, M.; Hu, S.; Zhang, J.; Meng, S. Photoexcitation in Solids: First-Principles Quantum Simulations by Real-Time TDDFT. *Adv. Theory Simul.* **2018**, *1*, 1800055.
- (36) Schelter, I.; Kümmel, S. Accurate evaluation of real-time density functional theory providing access to challenging electron dynamics. *J. Chem. Theory Comput.* **2018**, *14*, 1910–1927.
- (37) Pedersen, T. B.; Kvaal, S. Symplectic integration and physical interpretation of time-dependent coupled-cluster theory. *J. Chem. Phys.* **2019**, *150*, 144106.
- (38) Pedersen, T. B.; Kristiansen, H. E.; Bodenstein, T.; Kvaal, S.; Schøyen, Ø. S. Interpretation of coupled-cluster many-electron dynamics in terms of stationary states. *J. Chem. Theory Comput.* **2020**, *17*, 388–404.
- (39) Vila, F. D.; Rehr, J. J.; Kas, J. J.; Kowalski, K.; Peng, B. Real-time coupled-cluster approach for the cumulant Green’s function. *J. Chem. Theory Comput.* **2020**, *16*, 6983–6992.
- (40) Chen, M.; Lopata, K. First-Principles Simulations of X-ray Transient Absorption for Probing Attosecond Electron Dynamics. *J. Chem. Theory Comput.* **2020**, *16*, 4470–4478, PMID: 32470295.
- (41) Skeidsvoll, A. S.; Balbi, A.; Koch, H. Time-dependent coupled-cluster theory for ultra-fast transient-absorption spectroscopy. *Phys. Rev. A* **2020**, *102*, 023115.

- (42) Skeidsvoll, A. S.; Moitra, T.; Balbi, A.; Paul, A. C.; Coriani, S.; Koch, H. Simulating weak-field attosecond processes with a Lanczos reduced basis approach to time-dependent equation-of-motion coupled-cluster theory. *Phys. Rev. A* **2022**, *105*, 023103.
- (43) Schreder, L.; Lubert, S. Local approaches for electric dipole moments in periodic systems and their application to real-time time-dependent density functional theory. *J. Chem. Phys.* **2021**, *155*, 134116.
- (44) Mattiat, J.; Lubert, S. Recent progress in the simulation of chiral systems with real time propagation methods. *Helvetica Chimica Acta* **2021**, *104*, e2100154.
- (45) Ye, L.; Wang, H.; Zhang, Y.; Liu, W. Self-adaptive real-time time-dependent density functional theory for x-ray absorptions. *J. Chem. Phys.* **2022**, *157*, 074106.
- (46) Yang, M.; Sissay, A.; Chen, M.; Lopata, K. Intruder Peak-Free Transient Inner-Shell Spectra Using Real-Time Simulations. *J. Chem. Theory Comput.* **2022**, *18*, 992–1002, PMID: 35025498.
- (47) Saue, T. Relativistic Hamiltonians for chemistry: a primer. *Chem. Phys. Chem* **2011**, *12*, 3077–3094.
- (48) Heully, J. L.; Lindgren, I.; Lindroth, E.; Lundqvist, S.; Martensson-Pendrill, A. M. Diagonalisation of the Dirac Hamiltonian as a basis for a relativistic many-body procedure. *J. Phys. B: At. Mol. Phys.* **1986**, *19*, 2799–2815.
- (49) Jensen, H. J. A. "Douglas–Kroll the Easy Way", The Conference Talk, REHE 2005, Mülheim (Germany).
- (50) Kutzelnigg, W.; Liu, W. Quasirelativistic theory equivalent to fully relativistic theory. *J. Chem. Phys.* **2005**, *123*, 241102.
- (51) Liu, W.; Kutzelnigg, W. Quasirelativistic theory. II. Theory at matrix level. *J. Chem. Phys.* **2007**, *126*, 114107.

- (52) Ilias, M.; Saue, T. An infinite-order two-component relativistic Hamiltonian by a simple one-step transformation. *J. Chem. Phys.* **2007**, *126*, 064102.
- (53) Liu, W.; Peng, D. Exact two-component Hamiltonians revisited. *J. Chem. Phys.* **2009**, *131*, 031104.
- (54) Konecny, L.; Kadek, M.; Komorovsky, S.; Malkina, O. L.; Ruud, K.; Repisky, M. Acceleration of relativistic electron dynamics by means of X2C transformation: application to the calculation of nonlinear optical properties. *J. Chem. Theory Comput.* **2016**, *12*, 5823–5833.
- (55) Sikkema, J.; Visscher, L.; Saue, T.; Iliáš, M. The molecular mean-field approach for correlated relativistic calculations. *J. Chem. Phys.* **2009**, *131*, 124116.
- (56) Blume, M.; Watson, R. E. Theory of spin-orbit coupling in atoms I. Derivation of the spin-orbit coupling constant. *Proc. R. Soc. Lond. A* **1962**, *270*, 127–143.
- (57) Blume, M.; Watson, R. E. Theory of spin-orbit coupling in atoms, II. Comparison of theory with experiment. *Proc. R. Soc. Lond. A* **1963**, *271*, 565–578.
- (58) Heß, B. A.; Marian, C. M.; Wahlgren, U.; Gropen, O. A Mean-Field Spin-Orbit Method Applicable to Correlated Wavefunctions. *Chem. Phys. Lett.* **1996**, *251*, 365.
- (59) Schimmelpfennig, B. AMFI, an atomic mean-field spin-orbit integral program, 1996, University of Stockholm, Stockholm.
- (60) van Wüllen, C.; Michauk, C. Accurate and Efficient Treatment of Two-Electron Contributions in Quasirelativistic High-Order Douglas-Kroll Density-Functional Theory. *J. Chem. Phys.* **2005**, *123*, 204113.
- (61) Peng, D.; Liu, W.; Xiao, Y.; Cheng, L. Making Four- and Two-Component Relativistic Density Functional Methods Fully Equivalent Based on the Idea of from Atoms to Molecule. *J. Chem. Phys.* **2007**, *127*, 104106.

- (62) Boettger, J. C. Approximate Two-Electron Spin-Orbit Coupling Term for Density-Functional-Theory DFT Calculations Using the Dougl. *Phys. Rev. B* **2000**, *62*, 7809–7815.
- (63) Filatov, M.; Zou, W.; Cremer, D. Spin-orbit coupling calculations with the two-component normalized elimination of the small component method. *J. Chem. Phys.* **2013**, *139*, 014106.
- (64) Knecht, S.; Repisky, M.; Jensen, H. J. A.; Saue, T. Exact two-component Hamiltonians for relativistic quantum chemistry: Two-electron picture-change corrections made simple. *J. Chem. Phys.* **2022**, *157*, 114106.
- (65) Liu, J.; Cheng, L. An atomic mean-field spin-orbit approach within exact two-component theory for a non-perturbative treatment of spin-orbit coupling. *J. Chem. Phys.* **2018**, *148*, 144108.
- (66) Li, X.; Govind, N.; Isborn, C.; DePrince III, A. E.; Lopata, K. Real-time time-dependent electronic structure theory. *Chem. Rev.* **2020**, *120*, 9951–9993.
- (67) Repisky, M.; Konecny, L.; Kadek, M.; Komorovsky, S.; Malkin, O. L.; Malkin, V. G.; Ruud, K. Excitation energies from real-time propagation of the four-component Dirac–Kohn–Sham equation. *J. Chem. Theory Comput.* **2015**, *11*, 980–991.
- (68) Kadek, M.; Konecny, L.; Gao, B.; Repisky, M.; Ruud, K. X-ray absorption resonances near $L_{2,3}$ -edges from real-time propagation of the Dirac–Kohn–Sham density matrix. *Phys. Chem. Chem. Phys.* **2015**, *17*, 22566–22570.
- (69) De Santis, M.; Storch, L.; Belpassi, L.; Quiney, H. M.; Tarantelli, F. PyBERTHART: A relativistic real-time four-component TDDFT implementation using prototyping techniques based on python. *J. Chem. Theory Comput.* **2020**, *16*, 2410–2429.

- (70) Goings, J. J.; Kasper, J. M.; Egidi, F.; Sun, S.; Li, X. Real time propagation of the exact two component time-dependent density functional theory. *J. Chem. Phys.* **2016**, *145*, 104107.
- (71) Koulias, L. N.; Williams-Young, D. B.; Nascimento, D. R.; DePrince III, A. E.; Li, X. Relativistic real-time time-dependent equation-of-motion coupled-cluster. *J. Chem. Theory Comput.* **2019**, *15*, 6617–6624.
- (72) Konecny, L.; Komorovsky, S.; Vicha, J.; Ruud, K.; Repisky, M. Exact two-component TDDFT with simple two-electron picture-change corrections: x-ray absorption spectra near L- and M-edges of four-component quality at two-component cost. *J. Phys. Chem. A* **2023**, just accepted (DOI:10.1021/acs.jpca.2c08307).
- (73) Perfetto, E.; Stefanucci, G. Some exact properties of the nonequilibrium response function for transient photoabsorption. *Phys. Rev. A* **2015**, *91*, 033416.
- (74) Tannor, D. J. *Introduction to Quantum Mechanics: A Time-Dependent Perspective*; University Science Books: Sausalito, 2007; pp 185–196.
- (75) Norman, P.; Ruud, K.; Saue, T. *Principles and practices of molecular properties: theory, modeling, and simulations*; Wiley-VCH: Chichester, 2018.
- (76) Walkenhorst, J.; Giovannini, U. D.; Castro, A.; Rubio, A. Tailored pump-probe transient spectroscopy with time-dependent density-functional theory: controlling absorption spectra. *Eur Phys J B* **2016**, *89*.
- (77) Castro, A.; Marques, M. A.; Rubio, A. Propagators for the time-dependent Kohn–Sham equations. *J. Chem. Phys.* **2004**, *121*, 3425–3433.
- (78) Gomez Pueyo, A.; Marques, M. A.; Rubio, A.; Castro, A. Propagators for the time-dependent Kohn–Sham equations: multistep, Runge–Kutta, exponential Runge–Kutta, and commutator free Magnus methods. *J. Chem. Theory Comput.* **2018**, *14*, 3040–3052.

- (79) Norman, P.; Dreuw, A. Simulating x-ray spectroscopies and calculating core-excited states of molecules. *Chem. Rev.* **2018**, *118*, 7208–7248.
- (80) Kasper, J. M.; Stetina, T. F.; Jenkins, A. J.; Li, X. Ab initio methods for L-edge x-ray absorption spectroscopy. *Chem. Phys. Rev.* **2020**, *1*, 011304.
- (81) Bokarev, S. I.; Kühn, O. Theoretical x-ray spectroscopy of transition metal compounds. *Wiley Interdiscip. Rev. Comput. Mol. Sci.* **2020**, *10*, e1433.
- (82) Besley, N. A. Modeling of the spectroscopy of core electrons with density functional theory. *Wiley Interdiscip. Rev. Comput. Mol. Sci.* **2021**,
- (83) Konecny, L.; Vicha, J.; Komorovsky, S.; Ruud, K.; Repisky, M. Accurate x-ray absorption spectra near L- and M-edges from relativistic four-component damped response time-dependent density functional theory. *Inorg. Chem.* **2021**, *61*, 830–846.
- (84) Repisky, M.; Komorovsky, S.; Kadek, M.; Konecny, L.; Ekström, U.; Malkin, E.; Kaupp, M.; Ruud, K.; Malkina, O. L.; Malkin, V. G. ReSpect: Relativistic spectroscopy DFT program package. *J. Chem. Phys.* **2020**, *152*, 184101.
- (85) Komorovsky, S.; Cherry, P. J.; Repisky, M. Four-component relativistic time-dependent density-functional theory using a stable noncollinear DFT ansatz applicable to both closed- and open-shell systems. *J. Chem. Phys.* **2019**, *151*, 184111.
- (86) Stanton, R. E.; Havriliak, S. Kinetic balance: A partial solution to the problem of variational safety in Dirac calculations. *J. Chem. Phys.* **1984**, *81*, 1910–1918.
- (87) Dunning Jr, T. H. Gaussian basis sets for use in correlated molecular calculations. I. The atoms boron through neon and hydrogen. *J. Chem. Phys.* **1989**, *90*, 1007–1023.
- (88) Kendall, R. A.; Dunning Jr, T. H.; Harrison, R. J. Electron affinities of the first-row atoms revisited. Systematic basis sets and wave functions. *J. Chem. Phys.* **1992**, *96*, 6796–6806.

- (89) Woon, D. E.; Dunning Jr, T. H. Gaussian basis sets for use in correlated molecular calculations. III. The atoms aluminum through argon. *J. Chem. Phys.* **1993**, *98*, 1358–1371.
- (90) Wilson, A. K.; Woon, D. E.; Peterson, K. A.; Dunning Jr, T. H. Gaussian basis sets for use in correlated molecular calculations. IX. The atoms gallium through krypton. *J. Chem. Phys.* **1999**, *110*, 7667–7676.
- (91) Adamo, C.; Barone, V. Toward reliable density functional methods without adjustable parameters: The PBE0 model. *J. Chem. Phys.* **1999**, *110*, 6158–6170.
- (92) Marques, M. A.; Castro, A.; Bertsch, G. F.; Rubio, A. octopus: a first-principles tool for excited electron–ion dynamics. *Comput. Phys. Commun.* **2003**, *151*, 60–78.
- (93) Castro, A.; Appel, H.; Oliveira, M.; Rozzi, C. A.; Andrade, X.; Lorenzen, F.; Marques, M. A.; Gross, E.; Rubio, A. Octopus: a tool for the application of time-dependent density functional theory. *Phys. Status Solidi B* **2006**, *243*, 2465–2488.
- (94) Tancogne-Dejean, N.; Oliveira, M. J.; Andrade, X.; Appel, H.; Borca, C. H.; Le Breton, G.; Buchholz, F.; Castro, A.; Corni, S.; Correa, A. A. et al. Octopus, a computational framework for exploring light-driven phenomena and quantum dynamics in extended and finite systems. *J. Chem. Phys.* **2020**, *152*, 124119.
- (95) Fuks, J. I.; Helbig, N.; Tokatly, I. V.; Rubio, A. Nonlinear phenomena in time-dependent density-functional theory: What Rabi oscillations can teach us. *Phys. Rev. B* **2011**, *84*, 075107.
- (96) Fuks, J. I.; Luo, K.; Sandoval, E. D.; Maitra, N. T. Time-resolved spectroscopy in time-dependent density functional theory: an exact condition. *Phys. Rev. Lett.* **2015**, *114*, 183002.

- (97) Fuks, J. I.; Lacombe, L.; Nielsen, S. E. B.; Maitra, N. T. Exploring non-adiabatic approximations to the exchange–correlation functional of TDDFT. *Phys. Chem. Chem. Phys.* **2018**, *20*, 26145–26160.
- (98) Baseggio, O.; Toffoli, D.; Stener, M.; Fronzoni, G.; de Simone, M.; Grazioli, C.; Coreno, M.; Guarnaccio, A.; Santagata, A.; D’Auria, M. S2p core level spectroscopy of short chain oligothiophenes. *J. Chem. Phys.* **2017**, *147*, 244301.